(Received 23 August 2026, Accepted 15 September 2026, Scheduled 24 September 2026)

Multi-Objective Optimization Strategy for Outer-Rotor Permanent Magnet Brushless DC Motors Based on EBF Surrogate Model and GRA-TOPSIS

Xiaoting Ye*, Xianhai Yu, Zirui Chen, and Tao Zhang

Faculty of Automation, Huai'an University, Huai'an 223003, China

ABSTRACT: This paper proposes a surrogate model-based multi-objective optimization framework to improve the comprehensive electromagnetic performance of outer rotor permanent magnet brushless DC motors. Targeting key performance metrics including efficiency, torque ripple, cogging torque, core loss, and total harmonic distortion (THD) of back-electromotive force (EMF), a parametric finite-element model is established to identify key parameters and performance indicators. Dimensionality reduction is carried out through statistical correlation and cluster analysis. We then construct an Elliptical Basis Functions (EBF) neural network surrogate model to replace the computationally expensive finite-element model. Different from conventional Response Surface Methodology (RSM) and Radial Basis Function (RBF) models, EBF adopts Mahalanobis distance to mitigate prediction deviation induced by parameter coupling and achieves superior fitting accuracy for strongly nonlinear motor responses under limited sample size. The Pareto solution set is obtained via the Non-dominated Sorting Genetic Algorithm (NSGA-II). Then, the GRA-TOPSIS multi-criteria decision-making approach is employed to objectively select the global optimal solution from the Pareto solution set and avoid subjective solution selection. Finite element analysis results confirm that the motor performance has been significantly improved: torque ripple, peak cogging torque, core loss, and eddy-current loss are reduced by 18.8%, 18.7%, 6.97%, and 7.12%, respectively, and the effectiveness of constructing an efficient optimization framework has been verified.

1. INTRODUCTION

As core equipment in industrial production and social operations, the energy efficiency and environmental performance of electric motors have emerged as a national strategic priority [1]. Brushless DC motors, with advantages such as high efficiency, reliability, and maintenance-free operation, see their key technological research playing a crucial role in advancing the energy consumption revolution [2].

Permanent magnet brushless DC motors (PMBLDCMs) are structurally categorized into outer-rotor and inner-rotor topologies. The outer-rotor permanent magnet brushless DC motor (ORPMBLDCM), characterized by its external rotor and internal stator configuration, shows enhanced performance metrics in low-speed, high-torque operational regimes compared to inner-rotor counterparts. The implementation of rare-earth permanent magnets in the rotor assembly facilitates superior power density and torque generation within compact form factors [3]. Nevertheless, vibrational acoustics impose significant constraints on ORPMBLDCM performance enhancement. This multivariable, strongly-coupled= nonlinear system necessitates parametric optimization of design variables including permanent magnet geometry and stator slot dimensions, rendering multi-objective optimization a critical research frontier [4]. Electromagnetic vibration origination mechanisms are principally attributed to cogging torque oscillations, torque ripple phenomena, back electromotive force (EMF) harmonic distortion, and waveform irregularities [5]. Despite finite element analysis (FEA) serving as an essential computational tool for motor performance characterization, iterative FEA evaluation brings heavy computational overhead and severely impedes optimization throughput [6]. Even for 2-D transient electromagnetic simulation of ORPMBLDCM, every single calculation consumes considerable runtime; repeated calls to FEA for multi-objective optimization will lead to prohibitive total time cost. A novel analytical approach addresses the low computational efficiency of FEA in cogging torque prediction [7]. However, model simplification may introduce potential precision trade-offs.

In recent years, to enhance permanent magnet motor optimization efficiency and accuracy, scholars have introduced novel methods such as the Taguchi method, Response Surface Methodology (RSM), sensitivity analysis, and multi-objective optimization algorithms [8]. In [9], a precise analytical method calculates motor parameters, and NSGA-II optimizes the design, reducing permanent magnet consumption and torque ripple. In [10], the Taguchi method and FEA optimize ORPMBLDCM, achieving low cogging torque and weight, and improved back EMF. In [11], RSM is constructed via sensitivity analysis and optimized with NSGA-II, validated by simulations and experiments. In [12], hierarchical optimization is adopted, using RSM and NSGA-II for high-sensitivity variables and single-parameter scanning for low-sensitivity ones. RSM's ef-

* Corresponding author: Xiaoting Ye (yxthyit@hyit.edu.cn).

fectiveness attracts scholars as it improves electromagnetic performance and reduces vibration. However, although RSM-based surrogate model is faster, it may lead to highly nonlinear output errors [13]. Neural networks have become a new strategy for motor optimization because of their nonlinear-mapping ability. In [14], although additional data collection is required, neural networks achieve accurate performance predictions by capturing complex motion-output relationships. In [15], embedded permanent-magnet motors are optimized using back propagation (BP) neural networks and NSGA-II, enhancing performance and efficiency. In [16], MIGA, RBF neural networks, and orthogonal experiments are used to reduce torque ripple in synchronous motors. In [17], Pareto optimization (RBFPO) based on elliptical basis neural networks is proposed. The power, efficiency, and weight of ORPMBLDCM are optimized taking into account geometric parameters, current density, and magnetic saturation.

Existing literature has demonstrated that the combination of RSM and NSGA-II, as well as RBF-based surrogate models, is widely adopted for permanent-magnet motor optimization. Nevertheless, two challenges remain unsolved for ORPMBLDCM optimization. First, for highly coupled motor design variables, many surrogate models require massive sample data to guarantee satisfactory prediction accuracy. Second, after obtaining Pareto non-dominated solution sets, the final optimal scheme is usually selected via empirical judgement, which introduces subjective bias. Therefore, it is of great engineering significance to develop an optimization framework that can deliver high-fidelity surrogate prediction under a limited sample budget and realize objective decision-making for Pareto solutions. To fill these research gaps for ORPMBLDCM, this paper proposes a multi-objective optimization strategy based on the EBF surrogate model and GRA-TOPSIS. Section 2 introduces its topological structure and parameters. Section 3 determines final input variables and optimization objectives via correlation and cluster analysis of design parameters and optimization objectives, the final input variables and optimization objectives. Section 4 establishes and verifies the EBF surrogate model and obtains the optimal solution in the Pareto solution by using NSGA-II and GRA-TOPSIS algorithms. Section 5 carries out finite element analysis verification on the optimized ORPMBLDCM. Section 6 gives the conclusion.

2. ORPMBLDCM STRUCTURE

In this paper, an ORPMBLDCM with a 14-pole, 12-slot structure is investigated, and its initial performance is accurately calculated using the magnetic circuit method. The main dimensions and performance parameters of the motor are calculated as

$$D_{is}^2 \alpha'_P n_1 = \frac{6.1P'}{L_{ef} A B_\delta k_w k_\phi} \tag{1}$$

where α' and P' are calculated pole arc coefficient and calculated power; D_{is} is the stator's inner diameter; n_1 is the synchronous rotational speed; L_{ef} is the core's effective length; B_δ is the air gap flux density amplitude; A is the line load; k_w is the winding coefficient; and k_ϕ is the magnetic-field waveform coefficient.

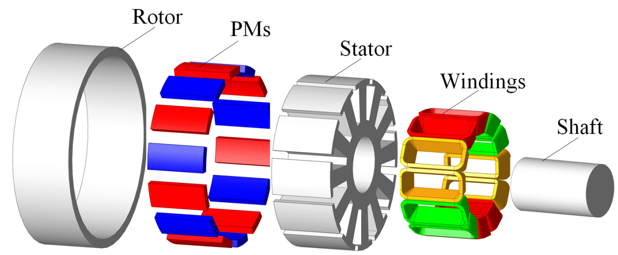

FIGURE 1. 3D topology model diagram of ORPMBLDCM.

Fig. 1 shows the structure of the ORPMBLDCM with a 14-pole, 12-slot. The motor is composed of an inner stator, an outer rotor, a three-phase winding, permanent magnets, and a rotating shaft. To realize a compact motor structure, a fractional-slot concentrated winding is utilized. The N35SH material is chosen for permanent magnets due to high residual magnetism and coercive force. Table 1 shows the motor's main design parameters and specifications.

TABLE 1. Main design parameters of ORPMBLDCM.

Parameters	Values
Pole/Slot	14/12
Rated power	75 W
Rated voltage	24 V
Rated Speed	2400 rpm
Outer diameter of stator	54 mm
Stator inner diameter	18 mm
Core Stack Thickness	20 mm
Permanent magnet materials	N35SH
Stator and rotor materials	DW315-50
Number of armature windings	30
Rotor outer diameter	66.5 mm
Phase number	3

3. OPTIMIZATION PARAMETER DETERMINATION AND DIMENSION REDUCTION ANALYSIS

3.1. Optimization Parameter Selection

To enhance the ORPMBLDCM's overall electromagnetic performance, multiple parameters for multi-objective optimization are used. The efficiency η is crucial as it directly links to energy consumption and economic benefits. Thus, efficiency optimization is prioritized. Efficiency can be derived from phase resistance, current, and various losses.

$$\eta = \frac{P_{out}}{P_{out} + P_{CoreLoss} + P_{cu} + P_s} \tag{2}$$

where P_{out}, $P_{CoreLoss}$, P_{cu}, and P_s are the motor's output power, core loss, winding copper loss, and stray loss, respectively.

Besides motor efficiency, torque quality is a key performance parameter. Using Maxwell's stress tensor method, the electromagnetic torque is given as

$$T_e(t) = \frac{L_{ef} R_e^2}{\mu_0} \int_{-\pi}^{\pi} B_r B_t d\theta = \sum_k T_k(t) \tag{3}$$

where L_{ef} is the effective axial length; R_e is the circumferential radius of the air gap; μ_0 is the vacuum conductivity; B_r and B_t are the radial and tangential magnetic densities, respectively; θ is the integration radian; and k is the number of air-gap harmonics.

The increase in torque may lead to a higher torque ripple that can cause vibration and noise. Reducing torque ripple is essential for better torque quality and overall performance. Torque ripple magnitude is written as

$$T_r = \frac{T_{\max} - T_{\min}}{T_{avg}} \times 100\% \tag{4}$$

where T_r, $T_{\max}$, $T_{\min}$, and T_{avg} are the torque ripple, maximum torque, minimum torque, and average torque value, respectively.

Cogging torque can indirectly induce torque ripple and speed fluctuations, resulting in motor vibration and noise. The cogging torque is given as

$$T_c(\alpha) = \frac{\pi z L_{ef}}{4\mu_0} \left(R_2^2 - R_1^2\right) \sum_{n=1}^{\infty} n G_n B_{r(nz/2p)} \sin(nz\alpha) \tag{5}$$

where p is the pole pair number; B_r is the residual magnetic flux density of the permanent magnet; μ_0 is the air-gap permeability; L_{ef}, R_2, and R_1 are the axial length of the armature core, the inner radius of the armature, and the outer radius of the rotor yoke, respectively; G_n is the Fourier decomposition coefficients of the air-gap flux density function; α is the relative position of the stator-rotor; and n is the number of permanent magnets.

Total Harmonic Distortion (THD) is also an indirect cause of motor torque ripple. Smaller THD results in a better sinusoidal waveform. When designing and optimizing an ORPMBLDCM, the THD of the back-EMF and radial air-gap magnets should be as small as possible to improve the motor's overall efficiency. THD can be expressed as

$$THD(\%) = \frac{\sqrt{\sum_{n=3,5,7,\ldots}^{\infty} C_n^2}}{C_1} \times 100\% \tag{6}$$

where C_1 and C_n are the fundamental and the nth harmonics of the back-EMF and air-gap magnetic density, respectively.

To comprehensively improve the motor's electromagnetic performance, efficiency (η), torque (T_e), torque ripple (T_r), iron loss ($P_{CoreLoss}$), cogging torque (T_c), peak-to-peak value of back EMF, back EMF $THD(EMF_{THD})$, radial air-gap magnetic density (Br), and air-gap magnetic density THD (Br_{THD}) are selected as optimization targets.

3.2. Motor Design Variables and Space Selection

ORPMBLDCM stator and rotor parameters can be used as optimization design variables. Slot height H_{s0}, slot shoulder depth H_{s1}, slot depth H_{s2}, slot width B_{s0}, upper slot shoulder width B_{s1}, lower slot shoulder width B_{s2}, rotor structure-related permanent magnet thickness Mt, air-gap length Ag, eccentricity H, and polar arc coefficient Eb are initially selected. To facilitate the subsequent optimization and analysis of the motor's structural parameters, it is necessary to parameterize the relevant structural parameters in the motor's finite element model, as shown in Fig. 2.

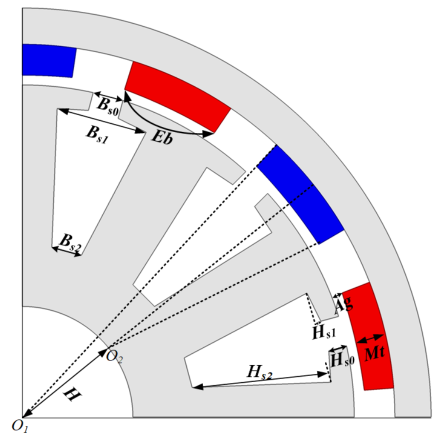

FIGURE 2. ORPMBLDCM parameterized model.

When selecting optimization variable design spaces, motor electromagnetic characteristics, mechanical properties, and processing difficulty are taken into account. Variable ranges are initially set by single-parameter scanning. Due to the topological constraints, the initial design space ranges from ±10% to ±30% of known values, determined by parameter importance. Table 2 shows initial values and reasonable ranges of variation for design parameters.

TABLE 2. ORPMBLDCM range of variation and initial values of design parameters.

Design parameters	Variable range	Initial value
Ag	[0.7 mm, 0.9 mm]	0.8 mm
B_{s0}	[1 mm, 3.5 mm]	2.5 mm
B_{s1}	[6.5 mm, 8.5 mm]	7.5 mm
B_{s2}	[2 mm, 3.5 mm]	2.5 mm
Eb	[0.6 mm, 0.8 mm]	0.65 mm
H_{s0}	[1 mm, 2 mm]	1.5 mm
H_{s1}	[0.2 mm, 1 mm]	0.5 mm
H_{s2}	[10.5 mm, 12.5 mm]	11 mm
H	[13.5 mm, 16.5 mm]	15 mm
Mt	[2 mm, 3.5 mm]	2.5 mm

3.3. Dimension Reduction Analysis

There are 10 optimized design parameters, resulting in complex calculations, stronger coupling effects, and difficult data processing. Some parameters have little impact on the response. To find the relationship between parameters and design indices, the Spearman rank correlation coefficient is used [18]. The correlation between design parameters and optimization goals is measured. Relevant design variables are selected. This coefficient is applicable to paired or continuous graded data.

$$\begin{cases} d_{ij} = x_i - y_j \\ \rho_{ij} = 1 - \frac{6 \sum\limits_{i=1,j=1}^{n,m} d_{ij}^2}{(n+m)\{(n+m)^2-1\}} \end{cases} \tag{7}$$

where x_i and y_j are rankings of the design parameters and optimization target samples, respectively; d_{ij} represents the difference in rank between the ith design parameter and the jth optimization criterion value; n and m signify the total number of design parameters and the set of optimization target samples, respectively.

The Spearman rank correlation coefficient ranges from -1 to 1. The closer the value is to the endpoints, the stronger the correlation between the design parameters and the optimization goal. Considering medium correlation, problem-complexity simplification, accuracy-efficiency balance, and engineering practice experience, the coefficient threshold is set at ± 0.5.

Figure 3 shows the result of the Spearman rank correlation coefficient. According to the threshold, it can be seen that the highly correlated parameters that affect the optimization targets include *Eb*, *Mt*, H_{s2}, H_{s0}, B_{s0}, and B_{s1}. *Ag*, H_{s1}, B_{s2}, and H are the low-correlated design parameters. To simplify the subsequent multi-objective optimization process, the parameters with weak correlation with all objectives are fixed to their initial values, and only strongly correlated structural parameters are selected for iterative optimization.

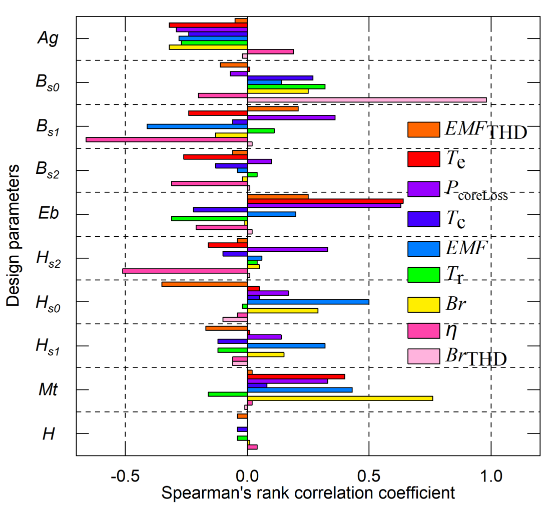

FIGURE 3. Parameter rank correlation analysis results.

In multi-objective optimization, the nine objectives of ORPMBLDCM show both correlation and competition, which complicates the optimization process. Complete-linkage agglomerative hierarchical clustering analysis quantifies objectives, eliminates redundancy, and balances conflicts with computational efficiency. Hierarchical clustering is a commonly used unsupervised learning approach, and complete-linkage is one of its linkage strategies [19]. The principle involves treating each data point as an independent cluster, using Euclidean distance as a measure of similarity, merging the two clusters with the smallest distance, and repeating this process until all objectives are in a single cluster. Finally, the average Pearson correlation coefficient within the cluster is calculated, and objectives with higher average values are considered redundant.

$$\begin{cases} d(C_i, C_j) = \max\limits_{1 \le k \le n_i, 1 \le l \le n_j} \{d(x_k, y_l)\} \\ R_{kl} = \frac{Cov(x_k, y_l)}{\sigma_{x_k} \sigma_{y_l}} \end{cases} \tag{8}$$

where $d(C_i, C_j)$ is the maximum Euclidean distance between clusters C_i and C_j; $d(x_k, y_l)$ is the Euclidean aggregation distance between point x_k in cluster C_i and point y_l in cluster C_j; n_i and n_j are the number of points in clusters C_i and C_j, respectively; and $Cov(x_k, y_l)$ and $\sigma_{x_k}, \sigma_{y_l}$ denote the covariance and standard deviation between clusters x_k and y_l.

Figure 4 shows average complete-linkage clustering results. Optimization objectives are merged based on minimum similarity measures, with highly similar ones grouped. Values are Pearson correlation coefficients, showing variable similarity, where red is positive and blue negative. Among them, T_r, T_c, and Br_{THD}, as well as *EMF*, *Br*, and T_e, are grouped in the two closest clusters, which indicates a high degree of similarity and mutual substitutability between them. By calculating the average Pearson correlation coefficient of the final adjacent clusters after merging, it is determined that the values for T_c, T_r, and Br_{THD} are 0.277, 0.173, and 0.174, respectively. It is concluded that Br_{THD} can be considered a redundant objective and substituted by T_r and T_c. For EMF, *Br* and T_e, the values are 0.264, 0.338, and 0.308, respectively. It is suggested that EMF and *Br* can be regarded as redundant objectives and replaced by T_e.

From the above hierarchical-clustering and Pearson correlation analysis, objectives with high correlation and strong substitutability are excluded to reduce computational complexity and prevent information overlap. Specifically, Br_{THD}, EMF,

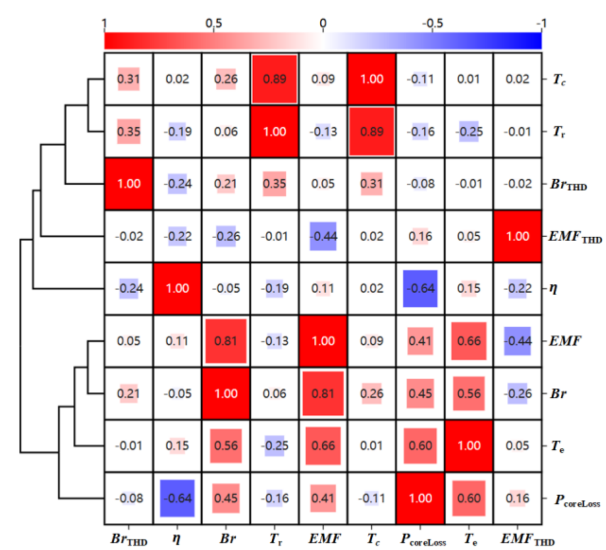

FIGURE 4. Results of average fully connected clustering method.

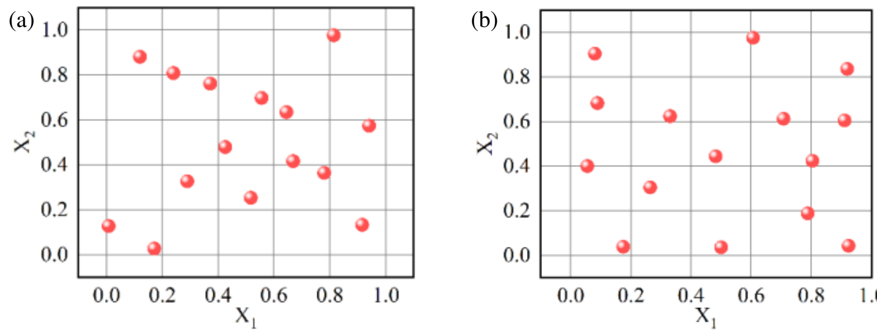

FIGURE 5. Comparison of sampling methods. (a) Normal LHD and (b) improved LHD.

and *Br* are highly correlated with T_r, T_c, and T_e and treated as redundant. Thus, six engineering-critical metrics are selected for multi-objective optimization: efficiency η, electromagnetic torque T_e, torque ripple T_r, cogging torque T_c, core loss $P_{CoreLoss}$, and back-EMF total harmonic distortion EMF_{THD}.

4. MULTI-OBJECTIVE OPTIMIZATION BASED ON EBF SURROGATE MODEL AND GRA-TOPSIS

4.1. Establishment of Motor Input and Output Sample Database

High-precision surrogate models rely on high-quality sample data. Although central composite design (CCD) and Box-Behnken design (BBD) are common in design of experiments (DOE), they are not ideal for multi-parameter and multi-objective scenarios. Instead, uniform design sampling, Latin hypercube design (LHD), and filled Latin hypercube are better [20]. To improve LHD, this paper applies criteria such as uniformity, space filling, and non-correlation as the sampling method. Fig. 5(a) shows that ordinary LHD has point clustering and gaps in 2D, resulting in uneven multi-dimensional coverage. Fig. 5(b) shows that the improved LHD adjusts points to achieve minimum correlation, better space filling, greater point distance, and more uniform distribution, reducing the redundancy of variable coupling. 350 groups of sample data are generated by co-simulation scripting of Maxwell and OptiSLang. The whole dataset is randomly partitioned: 300 samples are used for surrogate model training, and the remaining 50 samples are reserved as an independent out-of-sample cross-validation test set. Different from training-set fitting evaluation, the 50 held-out test samples are adopted to quantify the generalization capability of the constructed surrogate model, avoiding over-fitting risk.

4.2. BESTABLISHMENT and Evaluation of EBF Surrogate Model

EBF neural network model is used as a surrogate model for motor optimization in this paper. Compared with conventional RSM and standard RBF neural networks, EBF uses Mahalanobis distance instead of Euclidean distance. Mahalanobis distance accounts for covariance and coupling relationships among multi-dimensional design parameters. Since motor geometric variables show strong mutual coupling in this outer-rotor BLDC problem, EBF can mitigate adverse effects induced by parameter correlation and yield superior nonlinear mapping performance for highly coupled electromagnetic responses.

Taking the Mahalanobis distance between the measurement point and the sample point as the independent variable, it performs a nonlinear transformation on the input variables. The mathematical model is written as

$$\begin{cases} f_k = f\left(\|x-x_i\|_m\right) = (x-x_i)^T S^{-1}(x-x_i) \\ \qquad (i=1 \ldots N) \\ S = \frac{1}{N}\sum\limits_{i=1}^{N}(x_i-c)(x_i-c)^T \\ \sum\limits_{i=1}^{N} w_i = 0 \\ Z_k = \sum\limits_{i=1}^{N} w_i f_k(x_i) + w_{N+1} \end{cases} \tag{9}$$

where $\|x-x_i\|_m$ is the Mahalanobis distance between the point to be measured and the sample point; $(x-x_i)$ is the difference vector between the point to be measured x and the sample point x_i; S is the covariance matrix; c is the sample centroid; N is the number of samples; Z_k is the response of the kth output stratum; and w_i is the weight coefficient of the ith sample.

The surrogate model is established based on the approximation of the finite element calculation model. Therefore, there is an inherent error between the predicted value and the finite element calculation value. The coefficient of determination (R^2), Mean Absolute Error (MAE), and Root Mean Square Error (RMSE) are adopted to evaluate the consistency between the constructed surrogate model and the actual sample points. The closer the R^2 value is to 1 and RMSE and MAE are to 0, the closer the surrogate model approximates the real model.

$$\begin{cases} RMSE = \sqrt{\frac{1}{h}\sum\limits_{i=1}^{h}\left(F_i-\hat{F}_i\right)} \\ R^2 = 1 - \frac{\sum\limits_{i=1}^{h}\left(F_i-\hat{F}_i\right)^2}{\sum\limits_{i=1}^{h}\left(F_i-\bar{F}_i\right)^2} \\ MAE = \frac{1}{h}\sum\limits_{i=1}^{h}\left|F_i-\hat{F}_i\right| \end{cases} \tag{10}$$

where h is the number of samples in the cross-validation test set; F_i is the calculated value of the actual model; $\hat{F}_i$ is the predicted

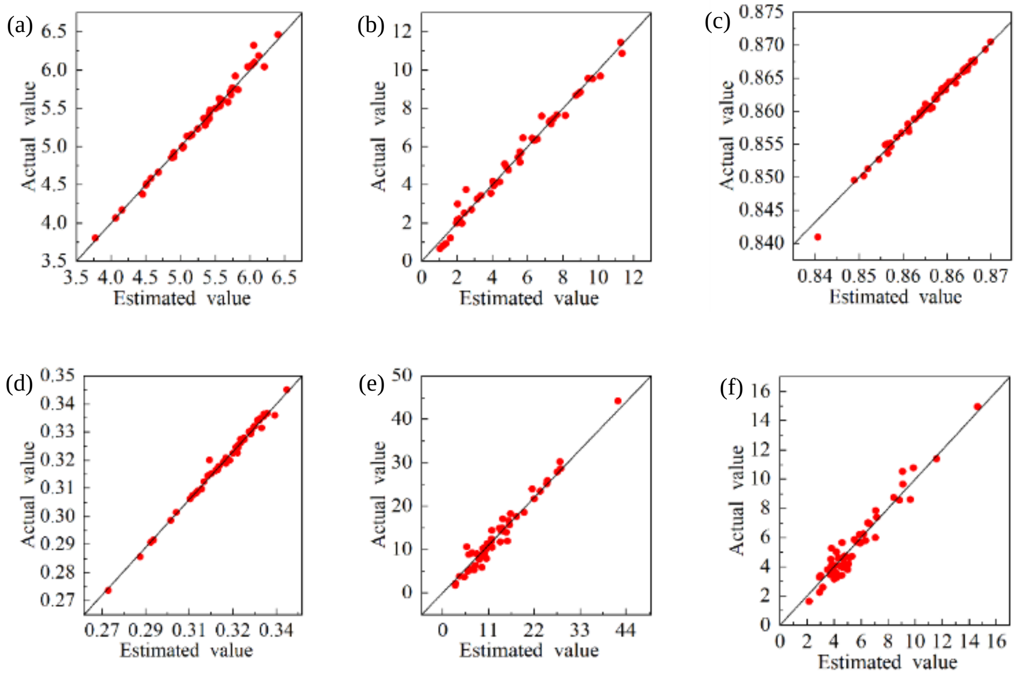

FIGURE 6. Results of target value prediction accuracy. (a) $P_{CoreLos}$, (b) EMF_{THD}, (c) η, (d) T_e, (e) T_c, and (f) T_r.

TABLE 3. EBF surrogate model error assessment.

Evaluation factor	Objectives					
	$P_{CoreLoss}$	EMF_{THD}	η	T_e	T_c	T_r
R^2	0.988	0.984	0.991	0.99	0.952	0.908
MAE	0.016	0.022	0.012	0.038	0.012	0.047
RMSE	0.024	0.032	0.018	0.055	0.019	0.064

value of the surrogate model; and $\bar{F}_i$ is the approximate average value of the sample points.

Using Maxwell and OptiSlang scripts, a sample set of 350 was obtained. The data set is imported into Isight to construct an EBF neural network model (6 selection objects, 6 design parameters). The sample space is split into training and test sets (50 test groups). Fig. 6 shows the comparison of actual predicted values from 50 cross validations. Both the predicted and actual values are clustered around the function $y = x$, indicating that the constructed EBF surrogate model has high credibility. Table 3 lists accuracy evaluation values. R^2 is all above 0.9, indicating that the six surrogate models can replace the time-consuming finite element model for future optimization design without resampling. Note that torque ripple achieves the lowest $R^2 = 0.908$. As a composite nonlinear metric, it is sensitive to air-gap harmonics, local saturation, and FEA numerical noise, leading to greater fitting difficulty. Nevertheless, this accuracy is acceptable for engineering optimization. Minor prediction deviation does not distort the Pareto frontier or mislead optimization decisions, which is supported by FEA validation in Section 5.

4.3. Multi-Objective Optimization Decision Based on NSGA-II and GRA-TOPSIS

The motor's objective functions and related constraint conditions are as follows:

$$\min: \begin{cases} F_1\left(\vec{X}\right) = T_c,\ F_2\left(\vec{X}\right) = T_r,\ F_3\left(\vec{X}\right) = -T_e \\ F_4\left(\vec{X}\right) = -\eta,\ F_5\left(\vec{X}\right) = P_{CoreLoss},\ F_9\left(\vec{X}\right) \\ \quad = EMF_{THD} \end{cases} \tag{11}$$

$$s.t. \begin{cases} T_c - 9\,\text{mNm} \le 0,\ T_r - 5\% \le 0,\ T_e - 0.31\,\text{Nm} \ge 0 \\ \eta - 0.87 \ge 0,\ P_{CoreLoss} - 4.5W \le 0,\ EMF_{THD} - 1.5\% \\ \le 0 \\ X_{\min} \le X \le X_{\max} \end{cases} \tag{12}$$

$$\vec{X} = (Eb, Mt, H_{s0}, H_{s2}, B_{s0}, B_{s1}) \tag{13}$$

To achieve the minimum optimization of the optimization goal, negative output torque (T_e), negative efficiency (η), and negative back EMF are used.

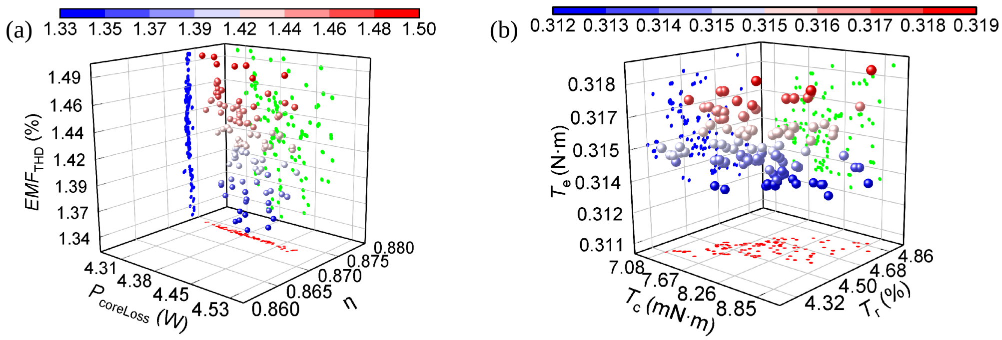

FIGURE 7. Pareto frontier solution set for the optimization objective.

After defining variables, constraints, and objectives and building a model, the non-dominated sorting genetic algorithm NSGA-II is selected to optimize the EBF surrogate model on the Isight platform. NSGA-II can effectively generate Pareto solutions with good diversity. Referring to widely adopted empirical parameter settings reported in existing multi-objective motor-optimization literature, the initial population size is set to 80; the maximum number of iterations is 50; the crossover rate is 0.9; and the mutation rate is 0.1. Fig. 7 presents the final result. After eliminating infeasible solutions, the optimization algorithm successfully generated a Pareto solution set containing 133 non-dominated solutions.

Identifying the comprehensive optimal solution from the multi-objective Pareto frontier is crucial for research and production. Traditional methods like random selection and the analytic hierarchy process are subjective. Grey relational analysis (GRA) and technique for order preference by similarity to an ideal solution (TOPSIS) are combined to scientifically evaluate the Pareto set for motor optimization. Their combination objectively calculates the grey relational degree, finds the optimal solution, offers a scientific basis for motor optimization, and overcomes drawbacks of traditional approaches. The calculation steps are given as follows:

(1) Assume that the decision-making model contains m evaluation entities and n assessment criteria, and construct the original optimization objective data matrix $X = [x_{ij}]_{mn}$ $(i = 1, 2, ..., m;\ j = 1, 2, ..., n)$. According to the nature of the optimization objectives, the max-min method is applied to the normalization of the data matrix.

(2) To avoid normalization issues and computational errors from zero elements in the optimization objective matrix, the lowest normalization interval begins at 0.002. This lower limit parameter has strong robustness with small fluctuations around 0.002, which is the optimal value that balances numerical stability and information retention. The method is written as

$$y_{ij} = \frac{[\max(z) - \min(z)] * \left[x'_{ij} - \min\left(x'_j\right)\right]}{\max\left(x'_j\right) - \min\left(x'_j\right)} + \min(z) \quad (14)$$

(3) Assume that the indicator matrix after normalization of the positivity is $Y = [y_{ij}]_{mn}$, and obtain positive and negative ideal solution vectors

$$\begin{cases} Y^+ = \{\max(\mathbf{y_{1j}}), \max(\mathbf{y_{2j}}) \cdots, \max(\mathbf{y}_{m\mathbf{j}})\}^T \\ Y^- = \{\min(\mathbf{y_{1j}}), \min(\mathbf{y_{2j}}) \cdots, \min(\mathbf{y}_{m\mathbf{j}})\}^T \end{cases} \quad (15)$$

(4) Generate positive and negative ideal solution absolute value indicator matrices $H^+ = [|Y - Y^+|]_{mn} = \left[\left|h_{ij}^+\right|\right]_{mn}$ and $H^- = [|Y - Y^-|]_{mn} = \left[\left|h_{ij}^-\right|\right]_{mn}$ and minimum values $t_{\min}^+$, $t_{\min}^-$ from matrices H^+ and H^- separately. Then, the gray correlation coefficient matrices $K^+ = \left[k_{ij}^+\right]_{mn}$ and $K^- = \left[k_{ij}^-\right]_{mn}$ of positive and negative ideal solutions are calculated.

$$\begin{cases} k_{ij}^+ = \frac{t_{\min}^+ + \rho t_{\max}^+}{h_{ij}^+ + \rho t_{\max}^+} \\ k_{ij}^- = \frac{t_{\min}^- + \rho t_{\max}^-}{h_{ij}^- + \rho t_{\max}^-} \end{cases} \quad (16)$$

where ρ is the resolution factor, generally set as 0.5.

(5) Calculate and score gray correlation scores ε_j^+ and ε_j^- for positive and negative ideal solutions:

$$\begin{cases} \varepsilon_j^+ = \frac{\sum_{i=1}^m k_{ij}^+}{m}, \quad \varepsilon_j^- = \frac{\sum_{i=1}^m k_{ij}^-}{m} \\ Score_j = \frac{1}{1 + (\varepsilon_j^- / \varepsilon_j^+)} \end{cases} \quad (17)$$

In this work, equal weighting is assigned to all optimization criteria in the GRA-TOPSIS decision process. Table 4 shows the calculation results of GRA-TOPSIS, and the optimal design point is the highest score 122nd law of the vital few solutions. Table 5 lists the data of design parameters before and after optimization.

TABLE 4. Results of GRA-TOSIS calculations.

No.	ε_j^+	ε_j^-	$Score_j$
1	0.6349	0.5103	0.3073
2	0.6164	0.5178	0.2953
3	0.5518	0.6025	0.2285
4	0.5519	0.6023	0.2286
⋮	⋮	⋮	⋮
120	0.6098	0.5612	0.2711
121	0.5363	0.6852	0.1927
122	0.7275	0.4824	0.3615
⋮	⋮	⋮	⋮
131	0.6588	0.562	0.2912
132	0.6325	0.5054	0.3089
133	0.5754	0.5871	0.2449

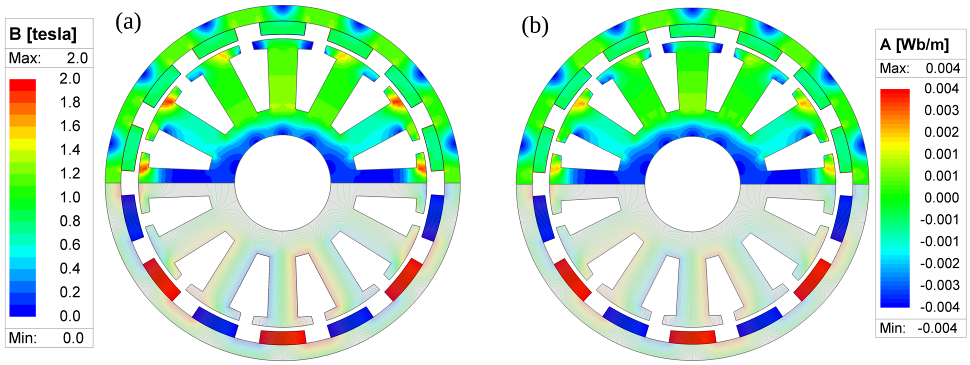

FIGURE 8. Magnetic field distribution before and after optimization. (a) Before optimization and (b) after optimization.

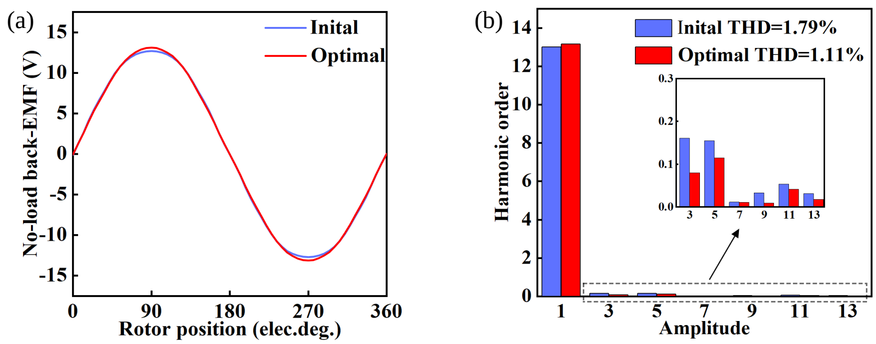

FIGURE 9. No-load back EMF and corresponding FFT analysis before and after optimization. (a) Back EMF and (b) FFT analysis.

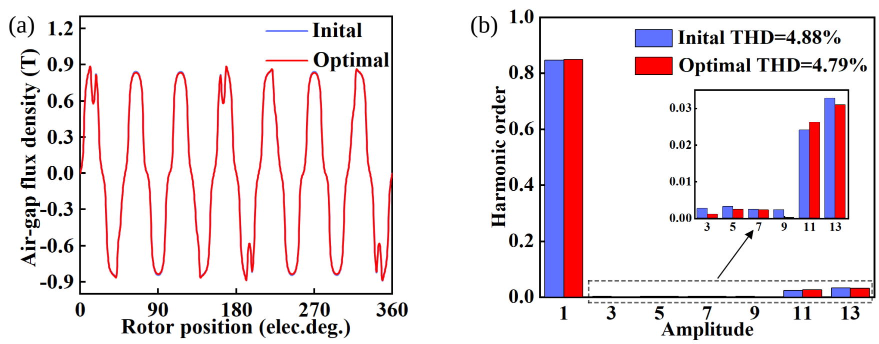

FIGURE 10. Air-gap flux density and corresponding FFT analysis before and after optimization. (a) Air-gap flux density and (b) FFT analysis.

TABLE 5. Comparison of optimized parameters.

Parameters	Before optimization	After optimization
B_{s0}	2.5 mm	2.49 mm
B_{s1}	7.5 mm	6.82 mm
Eb	0.65	0.66
H_{s0}	1.5 mm	1.7 mm
H_{s2}	11 mm	10.53 mm
Mt	2.5 mm	2.4 mm

5. ELECTROMAGNETIC PERFORMANCE ANALYSIS AND VALIDATION

To verify the effectiveness of the proposed method, the electromagnetic performance under no-load and load conditions is compared via finite element analysis. Table 6 shows the results. The optimized predicted value is close to the actual one. Figs. 8 to 12 compare the motor's electromagnetic performance.

Figure 8 shows the transient-field distribution and the motor's magnetic flux density under two design variables. The optimal parameters reduce leakage flux between the magnetic poles and lower the magnetic flux density of the stator teeth and yoke to approximately 1.7 T, within material tolerance. Parameter variations of the stator and rotor have not adversely affected the magnetic-field performance, maintaining the motor's reasonable topology. Fig. 9 compares no-load back EMF and harmonic spectra of ORPMBLDCM under initial and optimal variables. The optimized back EMF shows a 3.5% increase, whereas the amplitudes of all harmonic components and the THD decrease. This improvement will contribute to enhancing the motor's starting performance and maximum torque output.

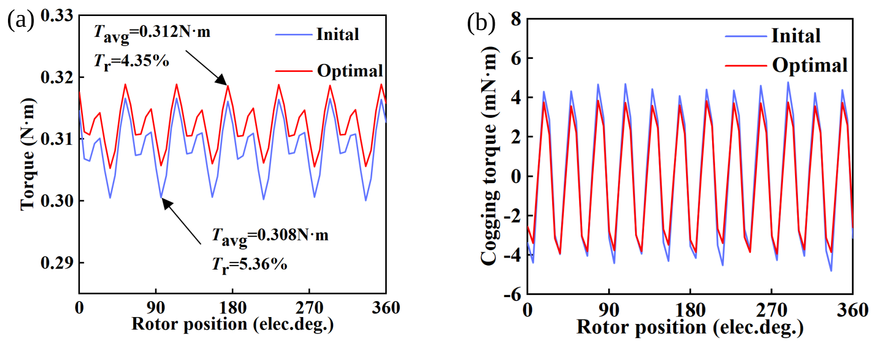

FIGURE 11. Torque and cogging torque before and after optimization. (a) Output torque and (b) cogging torque.

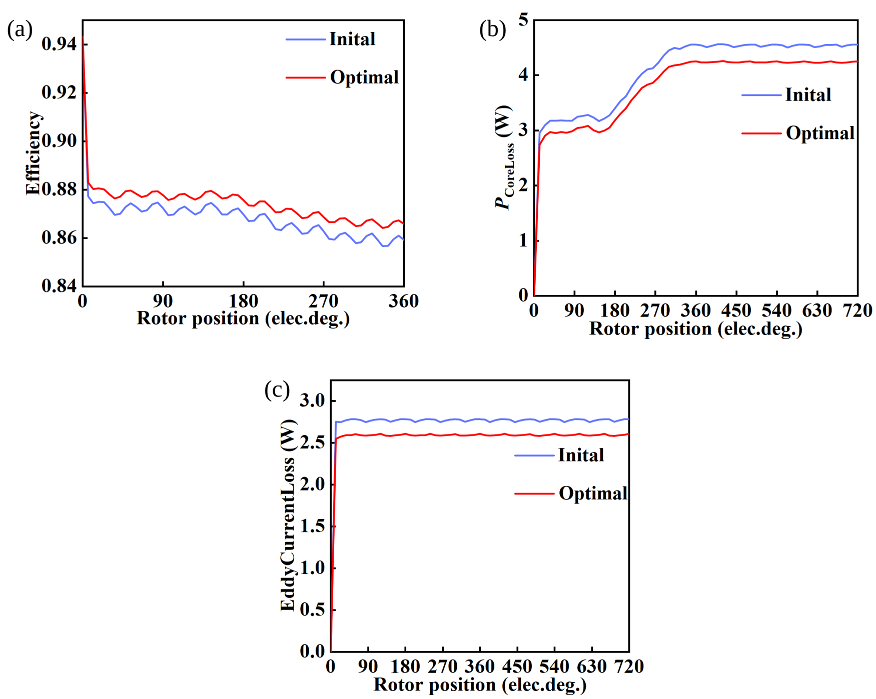

FIGURE 12. Efficiency and loss before and after optimization. (a) Efficiency, (b) core loss, and (c) eddy current loss.

TABLE 6. Performance comparison before and after motor optimization.

Objective	Initial value	Predicted value	Actual value
EMF_{THD}	1.79%	1.135%	1.111%
$P_{CoreLoss}$	4.59 W	4.289 W	4.272 W
η	0.868	0.873	0.874
T_e	0.308 Nm	0.312 Nm	0.312 Nm
T_r	5.358%	4.407%	4.350%
T_c	9.594 mNm	7.663 mNm	7.792 mNm
Br	1.775 T		1.773 T
Br_{THD}	4.84%		4.799%
EMF	25.348 V		26.236 V

Fig. 10 presents the air-gap magnetic flux density distribution and harmonic spectrum analysis. The optimized air-gap magnetic flux density stays mostly the same, but the 3rd, 5th, 7th, 9th, and 13th harmonics are notably decreased.

Figure 11(a) shows the optimized motor's output torque variation with rotor position under $id = 0$. With 4 A sinusoidal current injection, average output torque rises from 0.308 to 0.31 Nm, and torque ripple drops by 18.8% due to better back-EMF sinusoidality. Fig. 11(b) compares the cogging torques before and after optimization. The optimized peak cogging torque decreases from 4.797 to 3.896 mNm, achieving a reduction of 18.78%, which contributes to reducing torque ripple and noise. Fig. 12 shows efficiency, core loss, and eddy current loss. The instantaneous efficiency varies with rotor position. This phenomenon originates from the time-varying air-gap magnetic field and local magnetic saturation in stator/rotor iron, which yield position-dependent instantaneous core loss. Therefore, the average efficiency over one electrical period is used to assess steady-state motor performance. It can be seen that the efficiency increases from 86% to 87%. The core loss decreased from 4.59 to 4.27 W (a 6.97% reduction), and the eddy current loss decreased from 2.81 to 2.61 W (a 7.12% reduction), which validates the optimization method. Simulated results comprehensively prove the effectiveness of the multi-objective motor optimization design method.

6. CONCLUSION

This study proposes a multi-objective optimization strategy that combines the EBF surrogate model and the GRA-TOPSIS framework to improve the ORPMBLDCM's comprehensive electromagnetic performance. Through dimension reduction based on the Spearman rank correlation coefficient and uniformly, fully connected clustering method, the single-sampling surrogate model meets precision requirements. Finite element analysis shows that the comprehensive performance of the optimized motor is improved. The proposed approach reduces computational cost. The torque ripple, peak cogging torque core loss, and eddy current loss are reduced by 18.8%, 18.7%, 6.97%, and 7.12%, respectively. In addition, the GRA-TOPSIS multi-criteria decision-making method is used to objectively select the global optimal scheme from the Pareto solution set. Meanwhile, this approach can also be extended to other types of motors, providing a new approach for optimizing motor performance.

ACKNOWLEDGEMENT

This work was supported in part by Major Projects of the Basic Science (Natural Science) Research Program in Jiangsu Higher Education Institutions (24KJA470002) and in part by Huaian City Key R&D Plan Projects (HAG202302).

REFERENCES

[1] Konijeti, K., S. N. Mali, and M. L. Bharathi, "Extraction of maximum power from solar with BLDC motor driven electric vehicles based HHO algorithm," *Advances in Engineering Software*, Vol. 170, 103137, August 2022.

[2] Apribowo, C. H. B., M. Ahmad, and H. Maghfiroh, "Fuzzy logic controller and its application in brushless DC motor (BLDC) in electric vehicle — A review," *Journal of Electrical, Electronic, Information, and Communication Technology*, Vol. 3, No. 1, 35, April 2021.

[3] Du, G., C. Hu, Q. Zhou, W. Gao, and Q. Zhang, "Multi-objective optimization for outer rotor low-speed permanent magnet motor," *Applied Sciences*, Vol. 12, No. 16, 8113, August 2022.

[4] Sato, H. and H. Igarashi, "Automatic design of PM motor using Monte Carlo tree search in conjunction with topology optimization," *IEEE Transactions on Magnetics*, Vol. 58, No. 9, 1–4, September 2022.

[5] Jo, S.-T., H.-S. Shin, Y.-G. Lee, J.-H. Lee, and J.-Y. Choi, "Optimal design of a BLDC motor considering three-dimensional structures using the response surface methodology," *Energies*, Vol. 15, No. 2, 461, January 2022.

[6] Cheng, M., X. Zhao, M. Dhimish, W. Qiu, and S. Niu, "A review of data-driven surrogate models for design optimization of electric motors," *IEEE Transactions on Transportation Electrification*, Vol. 10, No. 4, 8413–8431, December 2024.

[7] Park, Y.-U. and D.-K. Kim, "Analytical prediction of the cogging torque in external-rotor single-phase BLDC motors with tapered air-gap," *International Journal of Applied Electromagnetics and Mechanics*, Vol. 59, No. 2, 721–728, February 2019.

[8] Cao, Y., L. Feng, R. Mao, L. Yu, H. Jia, and Z. Jia, "Multi-objective stratified optimization design of axial-flux permanent magnet memory motor," *Proceedings of the CSEE*, Vol. 41, No. 6, 1983–1991, 2021.

[9] Jing, Y.-Y., B. He, X.-Y. Yang, and Z.-M. Ma, "Multi objective optimization of outer rotor wheel-hub permanent magnet synchronous motor based on exact analytical method," *Journal of Electrical Engineering & Technology*, Vol. 19, No. 1, 507–519, June 2023.

[10] Ajamloo, A. M., A. Ghaheri, and E. Afjei, "Multi-objective optimization of an outer rotor BLDC motor based on taguchi method for propulsion applications," in *2019 10th International Power Electronics, Drive Systems and Technologies Conference (PEDSTC)*, 34–39, Shiraz, Iran, February 2019.

[11] Geng, W., J. Wang, L. Li, and J. Guo, "Design and multiobjective optimization of a new flux-concentrating rotor combining Halbach PM array and spoke-type IPM machine," *IEEE/ASME Transactions on Mechatronics*, Vol. 28, No. 1, 257–266, February 2023.

[12] Wang, X., Y. Fan, X. Lu, Q. Chen, and C. H. T. Lee, "Multiobjective optimization of a dual stator brushless hybrid excitation motor based on response surface model and NSGA 2," *IEEE Transactions on Industry Applications*, Vol. 58, No. 5, 6105–6114, September 2022.

[13] Ye, X., H. Chen, H. Liang, X. Chen, and J. You, "Multi-objective optimization design for electromagnetic devices with permanent magnet based on approximation model and distributed cooperative particle swarm optimization algorithm," *IEEE Transactions on Magnetics*, Vol. 54, No. 3, 1–5, March 2018.

[14] Gao, Y., T. Yang, S. Bozhko, P. Wheeler, T. Dragicevic, and C. Gerada, "Neural network aided PMSM multi-objective design and optimization for more-electric aircraft applications," *Chinese Journal of Aeronautics*, Vol. 35, No. 10, 233–246, October 2022.

[15] Ai, Q., H. Wei, and Y. Zhang, "Optimal design for flux-intensifying permanent magnet machine based on neural network and multi-objective optimization," in *2020 4th CAA International Conference on Vehicular Control and Intelligence (CVCI)*, Vol. 6, 596–601, Hangzhou, China, December 2020.

[16] Hao, J., S. Suo, Y. Yang, Y. Wang, W. Wang, and X. Chen, "Optimization of torque ripples in an interior permanent magnet synchronous motor based on the orthogonal experimental method and MIGA and RBF neural networks," *IEEE Access*, Vol. 8, 27 202–27 209, February 2020.

[17] Rahmani, O., S. A. Sadrossadat, M. Noohi, A. Mirvakili, and M. Shams, "Radial basis function-based Pareto optimization of an outer rotor brushless DC motor," *International Journal of Numerical Modelling: Electronic Networks, Devices and Fields*, Vol. 37, No. 2, 1–15, January 2024.

[18] Zhao, P., X. Wang, H. Yu, and S. Lu, "Method for identifying current operating conditions of main motor of cement rotary kiln based on spearman rank correlation coefficient," in *2019 34rd Youth Academic Annual Conference of Chinese Association of Automation (YAC)*, 537–541, Jinzhou, China, June 2019.

[19] Murtagh, F. and P. Contreras, "Algorithms for hierarchical clustering: An overview," *WIREs Data Mining and Knowledge Discovery*, Vol. 2, No. 1, 86–97, December 2011.

[20] Garud, S. S., I. A. Karimi, and M. Kraft, "Design of computer experiments: A review," *Computers & Chemical Engineering*, Vol. 106, 71–95, November 2017.